X-ray narrow-line transition radiation source based on low-energy electron beams traversing a multilayer nanostructure

A. E. Kaplan, C. T. Law,* and P. L. Shkolnikov
Department of Electrical and Computer Engineering, The Johns Hopkins University, Baltimore, Maryland 21218
(Received 13 January 1995)

X-ray transition radiation can be generated by low-energy electrons traversing a periodic multilayered solid-state nanostructure. In this paper, we investigate how the photoabsorption and electron scattering losses affect the maximal power of that radiation, the required electron energy, and the optimal total length of such a structure. We show that a combination of materials with high and low atomic numbers can produce an intense x-ray radiation with very narrow spectral peaks at the atomic inner-shell absorption edges of the materials, due to resonant anomalous dispersion of refractive index. We find that the photoabsorption and electron scattering result in only moderate increase of required electron energy as compared with the ideal lossless case. The photoabsorption also puts a certain "ceiling" on the required electron energy. We demonstrate the feasibility of an inexpensive x-ray source with mega- (or submega-) eV electrons that can generate narrow-line x-ray radiation. Its brightness can be high enough to compete with synchrotron radiation for a number of applications.

PACS number(s): 41.60.−m, 07.85.Fv, 41.75.Fr, 87.59.−e

INTRODUCTION

An electron crossing the interface between two semi-infinite dielectrics with different dielectric constants, ε_1 and ε_2, emits electromagnetic radiation [1]. This so-called transition radiation (TR) differs from Cerenkov radiation in that TR is emitted even if the speed of the electron is less than the speed of light in both materials, and from the bremsstrahlung in that TR is not attributed to the change of the electron momentum. TR can be greatly enhanced by using a periodic multilayer medium (the so-called resonant TR) [2–5] instead of a single interface, see Fig. 1. Spatial intensity distribution of resonant TR is conical, with most of the intensity at each particular wavelength λ concentrating near a certain emission angle θ measured from the electron velocity. Each TR spatial mode with a number r has a different resonant angle θ_r related to the wavelength λ and to the electron velocity v by the resonant condition

$$\overline{\varepsilon^{1/2}} \cos \theta_r = c/v - r\lambda/l, \tag{1}$$

where $\overline{\varepsilon^{1/2}} = (\sqrt{\varepsilon_1} l_1 + \sqrt{\varepsilon_2} l_2)/l$ is the mean refractive index of the medium, l_1 and l_2 are the thicknesses of different individual layers, and $l = l_1 + l_2$ is the spatial period. Equation (1) provides the condition for a constructive coherent interference of electromagnetic waves generated at different interfaces, at a distant point [see below, Eqs. (12) and (12′)]. The coherent interaction was explicitly demonstrated in the experiments [6] with a small number of layers, relatively high electron energy $E_0 \sim 17$–200 MeV, and $l \gg \lambda$. Furthermore, in most of the research on the resonant TR, even more energetic, ultrarelativistic electrons with energies $E_0 \sim 200$ MeV–50 GeV are used [2,3,7–9], which correspond to an even larger ratio l/λ [which scales as $\sim (E_0/mc^2)^2$].

On the other hand, with the presently available technologies, periodic multilayered structures can be readily manufactured with a spatial period on the nanometer scale (we will call them nanostructures), thus providing an opportunity to use much *lower* electron energies to obtain resonant TR as was proposed in Ref. [10] (see also [11,12]). In particular, it was shown [10] that with spatial period $l \leqslant 500$ Å electron energy of a few tens of keV, or even lower, satisfies the condition (1). Experiments with such multilayer nanostructures are further facilitated by the fact that they are well explored and conventionally used as x-ray mirrors in the same frequency domain [13]. We will show that for $E_0 \sim 0.5$–5 MeV the optimization of the TR efficiency at absorption edges yields optimal medium periods that are somewhat longer (~ 1000–1500 Å) but still orders of magnitude smaller than the thickness of the foils (and most of their spatial periods) used in the majority of TR experiments.

In the previous work [10–12], resonant TR was treated

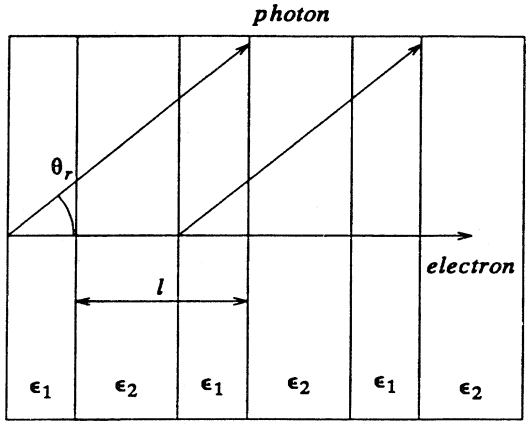

FIG. 1. The configuration of resonant TR.

*Present address: Department of Electrical Engineering and Computer Science, University of Wisconsin at Milwaukee, Milwaukee, WI 53201.

without taking photoabsorption and electron scattering into consideration. In solids, however, too slow electrons ($E_0<50-100$ keV) may be ineffective because of electron scattering. In this paper we show that, fortunately, a moderate increase in the electron energy above this level will render the loss of electrons insignificant. After taking both photoabsorption and electron scattering into consideration [14], we obtain the optimal range of electron energy (10^5-10^7 eV), the optimal total thickness of the superlattice, and maximal radiation for each given frequency ω. We show that up from $E_0\approx 100-200$ keV, the effect of photoabsorption of TR is stronger than that of electron scattering for most materials and frequencies. Indeed, the photoabsorption length is of the order of micrometers at wavelengths about 10 Å [15], whereas the half-critical length for electron scattering [16–18] is of the order of micrometers at $E_0=100$ keV and rapidly increases to millimeters at $E_0=1$ MeV. When the electron energy increases, the radiation at each frequency increases as well [3]. However, due to photoabsorption [14], increase in electron energy above a certain "ceiling" does not result in the increase of TR output. For typical absorption, this energy "ceiling" for $\lambda>10$ Å is 2–15 MeV.

TR is generated due to the difference in dielectric constants of adjacent layers, so that radiation power is proportional to $[\varepsilon_1(\omega)-\varepsilon_2(\omega)]^2$. Therefore, dispersion of the materials strongly affects the radiation intensity and spectrum. In systems utilizing ultrarelativistic electrons [7–9], light elements with small atomic number are used as radiators whereas air is a spacer. To employ low-energy electrons, solid-state nanostructures have to be used [10]. Since $|\varepsilon-1|$ is roughly proportional to the electron density, which increases with the atomic number, heavy elements (i.e., those with large atomic numbers) as radiators and light elements as spacers can provide a larger quantity $|\varepsilon_1-\varepsilon_2|$, at least at short wavelengths. Using materials with large atomic numbers is further justified by the fact that many absorption lines of these materials fall within the soft-x-ray domain, 0.1–2 keV [15], although these structures can also be used for the applications requiring harder x-rays, e.g., with energy ~30–35 keV needed for multiple-energy computed tomography (see Sec. VII), in which case K shells can be employed.

One of the major factors we consider here (see Sec. III) in applications to TR in solid-state nanostructures is the proposed use of very narrow spectral resonances of the dielectric constant of the atomic inner-shell (in particular, K, L, and M shells) absorption edges of the constituent materials. It is well known that due to photoionization of bound electrons, the absorption spectra of atoms in the x-ray domain show almost discontinuous jumps at the so-called absorption edges. This phenomenon is widely used in the experimental research and spectroscopic and radiation sources technology. However, a related phenomenon of strong resonances of a real component of dielectric constant ε at the absorption edges has never, to the best of our knowledge, been used in application to radiation sources. The resonant dispersion can result in ε significantly exceeding 1 at a resonance [in contrast to its regular plasmalike behavior in the x-ray domain, whereby $\varepsilon(\omega)<1$]. This strongly resonant anomalous x-ray dispersion of $\varepsilon(\omega)$ results in drastic changes of $[\varepsilon_1(\omega)-\varepsilon_2(\omega)]$ at the absorption edges of both the materials, and thus facilitates the formation of strong TR lines at these resonances. An absorption edge itself is instrumental in further narrowing of TR lines.

In Sec. I we briefly review theory of TR in a lossless periodic medium. In Sec. II, we incorporate photoabsorption and electron scattering into TR theory by introducing appropriate models. The important parameters for electron scattering and photoabsorption are critical length and absorption coefficient, respectively. The total calculated radiation includes bremsstrahlung. In Sec. III we discuss resonant peaks of the dielectric constants at inner-shell photoabsorption edges. In Sec. IV, we discuss selection of appropriate materials for the multilayer nanostructure for a narrow-line radiation with a particular peak frequency. In Sec. V we describe maximizing TR intensity with respect to the spatial period and total length of the material for a given electron energy. In Sec. VI, we present some examples with C or B as spacers, and Eu, Ba, Ce, or Ge as radiators for generating wavelengths from 10 to 100 Å. Finally, in Sec. VII we explore the perspective applications of resonant TR x-ray sources, in particular, multiple-energy computed tomography.

I. TRANSITION RADIATION IN A PERIODIC NONABSORBING MEDIUM

In the following, we assume that an electron passes through a periodic structure composed of alternating parallel layers with thicknesses l_1 and l_2 and dielectric constants ε_1 and ε_2, respectively, in the direction normal to the interfaces, Fig. 1. Radiation generated when an electron crosses each interface sums up constructively in the far-field area if the resonant condition, Eq. (1), is satisfied. TR differential efficiency which is defined as the number of generated TR photons N per electron per unit solid angle Ω (1 sr) per unit interval of the TR frequency ω in a multilayer system can be expressed as [2–4,8]

$$d^2N/d\Omega d\omega = F_1F_2F_3. \tag{2}$$

Here F_1 is the differential efficiency of a single interface, F_2 reflects the contribution of a single plate (i.e., of the very first couple of adjacent interfaces), and F_3 represents the coherence summation of radiation from all the periods (i.e., couples of individual adjacent layers [19]); all of them are defined below.

The differential efficiency of a single interface is given by [3]

$$F_1=\alpha(\beta\Delta\varepsilon)^2\pi^{-2}\omega^{-1}|G|^2, \tag{3}$$

where $\Delta\varepsilon=\varepsilon_1-\varepsilon_2$, $\alpha=\frac{1}{137}$ is the fine structure constant, $\beta=v/c$, and G is a radiation pattern of a single interface. If an electron moves from material 1 into material 2, the forward radiation pattern (i.e., for $0\leq\theta\leq\pi/2$, where θ is the emission angle in radians) is as

$$G(\beta,\varepsilon_1,\varepsilon_2,\theta)=\frac{\sin\theta\cos\theta(1-\beta^2\varepsilon_2-\beta\sqrt{\varepsilon_1-\varepsilon_2\sin^2\theta})}{(1-\beta^2\varepsilon_2\cos^2\theta)(1-\beta\sqrt{\varepsilon_1-\varepsilon_2\sin^2\theta})(\varepsilon_1\cos\theta+\sqrt{\varepsilon_1\varepsilon_2-\varepsilon_1^2\sin^2\theta})}. \quad (4)$$

For backward radiation ($\pi/2\leq\theta\leq\pi$), one should replace $\beta\rightarrow-\beta$, $\varepsilon_1\leftrightarrow\varepsilon_2$, and $\theta\rightarrow\pi-\theta$ in Eq. (4). In this paper, we concentrate on TR in the x-ray domain, where $|\varepsilon_j-1|\ll1$. We are also interested in the electron energies, which although allowed to be in relativistic domain, are still not too high, which is the main reason to use solid-state nanostructures; as we will see below (Sec. V), the electron energies E_0 required to optimize the radiation do not exceed a few megavolts. Introducing a dimensionless electron energy:

$$\gamma=(1-\beta^2)^{-1/2},\quad [E_0=mc^2(\gamma-1)]$$

(where m is the rest mass of the electron), we will assume that in all the cases considered here, the electron energy is significantly below the Čerenkov limit, $\gamma^2\ll|\varepsilon_j-1|^{-1}$. Although $\varepsilon_j<1$ for most of the x-ray domain, and therefore the Čerenkov radiation for the respective frequencies cannot be excited for any electron energy, at some narrow resonances at inner-shell photoabsorption edges (see Sec. III), ε_j-1 could be positive, although still small. Thus, for the energies of interest, we can still presume that $\gamma^2\ll|\varepsilon_j-1|^{-1}$ [see also a discussion below, Eq. (8)], so that, except for $\theta\approx\pi/2$, Eq. (4) can readily be simplified to exclude ε_j:

$$G(\beta,\theta)=\frac{\sin\theta(1-\beta^2-\beta\cos\theta)}{2(1-\beta^2\cos^2\theta)(1-\beta\cos\theta)}. \quad (5)$$

Near $\theta=\pi/2$, the approximate Eq. (5) deviates significanly from the exact Eq. (4).The next approximation, obtained from Eq. (4) by introducing $\phi\equiv\theta-\pi/2$ and assuming $|\phi|\ll\pi/2$ and $\varepsilon_j|\ll1$ is

$$G\approx\frac{|\phi|(1-\beta^2)}{|\phi|+\sqrt{\phi^2+(\varepsilon_1-\varepsilon_2)\mathrm{sgn}(\phi)}} \quad (6)$$

where $\mathrm{sgn}(\phi)=1$ for $\phi\geq0$ and $\mathrm{sgn}(\phi)=-1$ otherwise. This equation reveals (see inset in Fig. 2) that the factor $|G|^2$ not only zeros out at $\phi=0$ ($\phi=\pi/2$), as is obvious from Eq. (4) as well, but also has a drastic feature: a narrow peak at $\phi=\phi_{pk}$,

$$\phi_{pk}\approx-\mathrm{sgn}(\phi)\sqrt{|\varepsilon_1-\varepsilon_2|}, \quad (6')$$

$|G(\phi_{pk})|\equiv G_{pk}\approx\gamma^{-2}$. For the assumed $|\varepsilon_j|\leq1$, ϕ_{pk} is the angle of the total internal reflection. This interesting (yet not broadly addressed) feature is, however, insignificant in the context of our work, since the respective radiation, which propagates almost parallel to the layers, contains only a small fraction of the total TR power and can be safely neglected here.

In general, the factor F_1, Eq. (5), depends on the emission angle θ in a complicated way. A simpler picture of TR ensues when both the speed of the electron and the frequency of radiation are small, in which case the single-interface spatial factor G corresponds to a dipole radiation pattern [20] with the single lobe, $G\approx(\frac{1}{2})\sin\theta$. However, at $\beta=(\sqrt{5}-1)/2=0.618$ ($E_0\approx138.7$ keV; see curve 1 in Fig. 1), it splits into two lobes, a new lobe peaking near $\theta=0$. Figure 2 depicts $|G|^2$ versus θ, Eq. (5), for various energies E_0. As electron energy increases further, the radiation concentrates in this new lobe, which eventually gives rise to a narrow cone with the angle of maximal radiation tending to zero. When $|\varepsilon_j-1|^{-1}\gg\gamma^2\gg1$, one can further simplify G as

$$G\approx-\theta(\gamma^{-2}+\theta^2)^{-2},\quad \theta\ll1 \quad (7)$$

so that the angle of maximum radiation is $\theta_{\text{max rad}}\approx1/(\gamma\sqrt{3})$. When the electron energy becomes sufficiently high, such that γ^{-2} is comparable with $|\Delta\varepsilon_j|$, where $\Delta\varepsilon_j\equiv\varepsilon_j-1$, Eq. (4) results, instead of Eq. (5), in the equation

$$G\approx-\theta[(\gamma^{-2}+\theta^2-\Delta\varepsilon_1)(\gamma^{-2}+\theta^2-\Delta\varepsilon_2)]^{-1},\quad \theta\ll1. \quad (8)$$

If at least one of $\Delta\varepsilon_j(\lambda)$ is positive for certain λ's, $\gamma_{\check{C}er}=(\Delta\varepsilon_j)^{-1/2}$ is the critical energy of Čerenkov radiation, and if $\gamma>\gamma_{\check{C}er}$, the Čerenkov critical angle is $\theta_{\check{C}er}=\sqrt{\gamma_{\check{C}er}^{-2}-\gamma^{-2}}$. Since in the x-ray domain this situation can occur only at very narrow resonances at inner-shell photoabsorption edges (see Sec. III), the Čerenkov radiation at these resonances may suggest an interesting source of resonant x-ray radiation (with a single material instead of layered structure), as well as new, "Čerenkov" spectroscopy, whereby, e.g., $(\Delta\varepsilon_j)_{max}$ at a specific resonance is measured by the minimal energy γ required to attain Čerenkov radiation. The energies of a few MeV of interest to us here are far

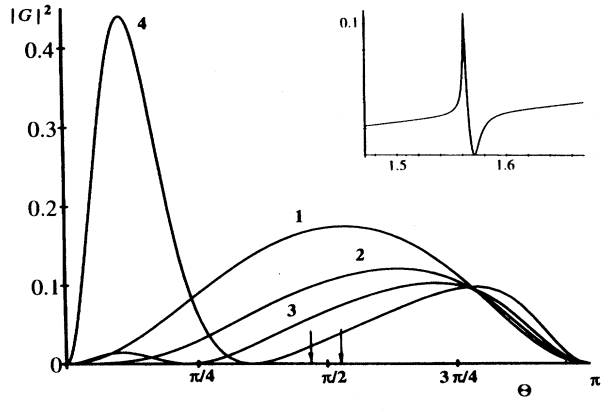

FIG. 2. Geometric factor $|G|^2$ for the single-interface TR [approximation, Eq. (5)] vs emission angle θ in radians for various electron energies E_0 (curve $1-E_0=10$ keV; curve 2, 125 keV; curve 3, 200 keV; and curve 4, 350 keV). Exact behavior of $|G|^2$ near $\theta=\pi/2$, in the region limited by the two arrows, is shown in the inset.

below Čerenkov critical energies (typically, a few hundred MeV), and thus Eqs. (5) and (7) can be used for our calculations throughout this paper.

The next factor in Eq. (2), F_2, is attributed to coherent summation of radiation generated at the very first couple of adjacent interfaces [3] (sandwiching usually the denser material), and assumes the interference pattern of two sources with different phases (one of them due to the propagation of the electromagnetic (EM) wave, and another due to a traversing electron; note also that the amplitudes of the waves radiated at these two interfaces have opposite signs due to switch of sign of $\Delta\varepsilon$ at the adjacent interfaces):

$$(F_2)_i = 4\sin^2(l_i/a_i), \quad i=1 \text{ or } 2. \tag{9}$$

Here i indicates which type of material makes the first layer, l_i is the thickness of that layer, and a_i is a respective "transformation length" of TR emitted from a single interface:

$$a_i = (\lambda/\pi)(\beta^{-1} - \sqrt{\varepsilon_i}\cos\theta)^{-1}. \tag{10}$$

For γ^{-2}, $|\Delta\varepsilon_i|$, $\theta^2 \ll 1$, this definition reduces to a more conventional expression

$$a_i \approx 2(\lambda/\pi)(\gamma^{-2} + \theta^2 - \Delta\varepsilon_i)^{-1} \tag{10'}$$

(see, e.g., [5]), or if $|\Delta\varepsilon_i|^{-1} \gg \gamma^2 \gg 1$, which is typically the case here,

$$a_1 \approx a_2 \approx 2(\lambda/\pi)(\gamma^{-2} + \theta^2)^{-1}. \tag{10''}$$

For an optimized angle of radiation, $\theta \approx \gamma^{-1}$ [see below, Eq. (45')], we have

$$a_1 \approx a_2 \approx \lambda\gamma^2/\pi,$$

e.g., for $\lambda = 10$ Å, $E_0 = 4.5$ MeV (i.e., $\gamma = 10$), one has $a_i \approx 320$ Å. When the resonant condition (1) is satisfied, and $|\Delta\varepsilon_i| \ll 1$, the factor F_2, Eq. (9), for the rth resonance reduces to

$$F_2 = 4\sin^2(\pi r l_2/l) = 4\sin^2(\pi r l_1/l), \tag{9'}$$

such that it makes no difference which material is first in the structure. Equations (9) and (9') indicate that the power radiated in a single plate is four times as large as the power generated at a single interface, when the interference is fully constructive. Starting from Sec. V, we will consider only the radiation at the first order ($r=1$) and always assume the optimally fabricated nanostructures with $l_1 = l_2$, such that $F_2 = 4$.

Finally, for a single electron traversing M periods, each period consisting of two adjacent layers of alternating *lossless* materials, the multilayer factor F_3 for coherent summation of TR from each period is [3,8]

$$F_3 = \sin^2(MX)/\sin^2(X), \tag{11}$$

where

$$X = l_1/a_1 + l_2/a_2 = l/\bar{a}, \tag{12}$$

with $\bar{a} = (\lambda/\pi)(\beta^{-1} - \bar{\varepsilon}^{1/2}\cos\theta)^{-1}$. If $\gamma^{-2} \ll |\Delta\varepsilon| \ll 1$, we have $\bar{a} \approx a_1 \approx a_2$, and

$$X \approx l\pi(\gamma^{-2} + \theta^2)/\lambda. \tag{12'}$$

X is a half-phase difference between each period [see Fig. 1 and Eq. (1)]. The factor F_3 peaks at $X = r\pi$ where $r = 1,2,3\ldots$, which results in the resonance condition, Eq. (1).

II. PHOTOABSORPTION AND ELECTRON SCATTERING

In the preceding section we discussed TR in the absence of the electron scattering and photoabsorption. This assumption is valid only for sufficiently high electron and photon energies. In any realistic multilayer system emitting soft-x-ray TR, however, photoabsorption and electron scattering significantly affect radiation. This is particularly true for a sub-MeV electron traversing solid-state structure (especially with high atomic numbers).

The multilayer enhancement of TR is expected only when losses due to both the photoabsorption and electron scattering are negligible within a single layer. Thus only the "multilayer" factor F_3 can be affected by those effects; the factors F_1 and F_2 remain intact. To account for the photoabsorption, we assume that the emitted field decays exponentially as $\exp[-\bar{\mu}z/(2\cos\theta)]$ where $\bar{\mu} = (\mu_1 l_1 + \mu_2 l_2)/l$ is the mean absorption coefficient, z is the distance traveled by the photon, and θ is the emission angle. With this model for absorption, a new factor $\tilde{F}_3$ has to be used instead of F_3 [14]:

$$\tilde{F}_3 = \left|\sum_{s=0}^{M-1} \Phi_s\right|^2, \quad \Phi_s = \exp[-\sigma(M-2) + 2iXs] \tag{13}$$

where Φ_s is the (normalized) contribution to the radiation field by the sth period. Introducing the dimensionless absorption parameter, $\sigma = \bar{\mu}l/(2\cos\theta)$, where the factor $\cos\theta$ in σ accounts for the longer path length traveled by radiation due to nonzero emission angle θ, one obtains [14]

$$\tilde{F}_3 = \frac{1 + e^{-2M\sigma} - 2e^{-M\sigma}\cos(2MX)}{1 + e^{-2\sigma} - 2e^{-\sigma}\cos(2X)}. \tag{14}$$

As expected, $\tilde{F}_3 = F_3$ when $\bar{\mu} = 0$. Equation (14) for $\tilde{F}_3$ is similar to the results [5,6] except for the factor $\cos\theta$ in G.

The electron scattering is a more complicated phenomenon than photoabsorption, and generally cannot be dealt with in a similar, straightforward way, using only one parameter. In the simplest approximation, any electron that has experienced a collision of any kind, whether elastic or inelastic, can simply be excluded from consideration. Therefore, in this approach, we retain for our calculations only that component of the initially monoenergetic and parallel electron beams that remains monoenergetic and parallel; however, the density of this component decreases as the beam propagates through the structure. This way, the attenuation of the electron beam is reflected only in the steadily decreasing number of generated TR photons. Such an approach is physically meaningful only if the probability of the scattering event is relatively small, which is typically the case [16,21,22]. Therefore, change in TR due to electron scattering can be

described by a single factor, transmission of electrons, T. This factor is then incorporated into $\tilde{F}_3$ by redefining Φ_s in Eq. (13) as

$$\Phi_s=\sqrt{T(z)}\exp[-\sigma(M-s)+2iXs], \tag{15}$$

with $T(z)$ interpreted here as the probability of an electron to pass unscattered through a distance z. The electron transmission T as a function of the material thickness can be characterized by a critical parameter $L_{\rm cr}$ defined as a distance at which virtually all electrons become scattered and/or absorbed. In terms of collision losses per unit path length, dE/dz, $L_{\rm cr}=E_0/(dE/dz)$ where E_0 is the energy of incident electrons. For a multilayer structure, one can define $L_{\rm cr}$ as $L_{\rm cr}=[(dE/dz)_1(l_1/l)+(dE/dz)_2(l_2/l)]$. In general, there are two major channels of collisional losses: electron-electron (or electron-plasmon) and electron-atom collisions. It is well known [16] that in the energy range of interest (200 keV and higher), the losses are mostly due to electron-atom collisions. The first-principle calculations of collision loss $(dE/dz)_i$ $(i=1,2)$ due to Bethe yield a formula [18,20,23]

$$\left(\frac{dE}{dz}\right)_i=2\pi m_0c^2r_e^2Z_i\beta^{-2}N_{Ai}\left[\ln\frac{(\gamma-1)^2(\gamma+1)}{2I_i^2}+\frac{(\gamma-1)^2/8-(2\gamma-1)\ln 2}{\gamma^2}+1-\beta^2\right], \tag{16}$$

where m_0 is the rest mass of the electron, $r_e=e^2/(m_0c^2)=2.82\times10^{-13}$ cm is the classical electron radius, e is the electron charge, $I_i=9.73Z_i+58.8Z_i^{-0.19}$ eV is the approximate ionization potential of the atom (for atomic number $Z_i>13$), and N_{Ai} are the atomic number densities. Quite a few simple empirical fits to either theoretical formulas such as Eq. (16) or to experimental data have been suggested, e.g. [24],

$$T=\exp[-\psi y/(1-y)], \tag{17}$$

where ψ is a fitting parameter that depends on the material, $y=z/L_{\rm cr}$ is the normalized penetration depth, z is the distance traveled by the electron. Equation (17), however, does not allow for an analytical expression for $\tilde{F}_3$ in Eq. (13). Instead, we propose the equation

$$\sqrt{T}=a_f-(a_f-1)\exp(\chi z), \tag{18}$$

where a_f is a fitting parameter and χ is a function of a_f, e.g., $\chi=-L_{\rm cr}^{-1}\ln[2(1-a_f^{-1})]$ for an abrupt fall of T at certain z with $1<a_f<2$. A few curves representing electron transmission for various values of a_f are depicted in Fig. 3. These curves are similar to those in Fig. 5 of Ref. [24]; however, T in the form of Eq. (18) gives us the advantage of making analytical calculations related to the TR with Eq. (13). In materials with high atomic numbers, electron transmission T decreases with distance almost linearly. In our model, Eq. (18), this property is best fitted if $a_f=2$ and $\chi=1/(2L_{\rm cr})$, i.e.,

$$\sqrt{T}=\begin{cases}2-e^{z/(2L_{\rm cr})}, & z<2L_{\rm cr}\ln 2\\ 0 \quad \text{otherwise.}\end{cases} \tag{19}$$

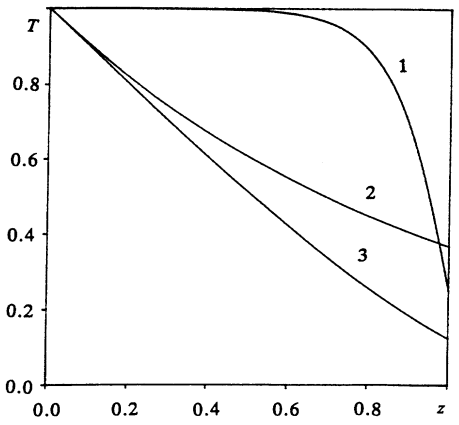

FIG. 3. Electron transmission T vs normalized distance z, according to Eq. (19). Curve 1, $a_f=10^{-5}$ with $\chi=\ln\{a_f/[2(a_f-1)]\}$; curve 2, $T=e^{-z}$; curve 3, $a_f=2$ with $\chi=1/(2\ln 2)$].

This function decreases almost linearly with distance for most of the interval $z<L_{\rm cr}$. Equations (13), (15), and (19) yield the factor $\tilde{F}_3$, which accounts for both photoabsorption and electron scattering:

$$\tilde{F}_3=2\pi e^{-2M\sigma}[4\phi(\tilde{M},\sigma)+\phi(\tilde{M},\sigma+\rho)-4\phi(\tilde{M},\sigma+\rho/2)], \tag{20}$$

where $\tilde{M}=M$ if $\rho\leq\ln 2$, and $\tilde{M}=2/\rho$ otherwise, and

$$\phi(u,\nu)\equiv\nu^{-1}\exp(u\nu)\sinh(u\nu), \quad \sigma\equiv\tilde{\mu}l/(2\cos\theta), \tag{20'}$$

$$\rho\equiv l/(2L_{\rm cr}).$$

Equation (20) reduces to Eq. (14) when $L_{\rm cr}\to\infty$. If $L_{\rm cr}$ is significantly larger than the total length of the multilayer structure (which is usually the case, see Sec. V), one can use a simpler yet, exponentially decaying function to approximate T, Eq. (18), in the limit $a\to\infty$,

$$T=\exp(-z/L_{\rm cr}). \tag{21}$$

This assumption is justified by the data for dE/dz in Ref. [16]. Consequently, instead of Eq. (20), we have a simpler expression:

$$\tilde{F}_3=e^{-(M-1)(\gamma+\rho)}\frac{\cosh[M(\sigma-\rho)]-\cos(2MX)}{\cosh(\sigma-\rho)-\cos(2X)}. \tag{22}$$

Combining the expressions in Eqs. (3), (12), and (22) for F_1, F_2, and $\tilde{F}_3$, respectively, we obtain the formula for the TR differential efficiency in the presence of both the photoabsorption and electron scattering for the rth mode:

$$\left(\frac{d^2N}{d\omega d\Omega}\right)_r = \frac{4\alpha(\Delta\beta)^2}{\pi^2\omega}|G|^2 \sin^2(l_2 r\pi/l) e^{-(M-1)(\gamma+\rho)} \frac{\cosh[M(\sigma-\rho)]-\cos(2MX)}{\cosh(\sigma-\rho)-\cos(2X)}. \tag{23}$$

The rapid variation of intensity with the angle θ in Eqs. (22) and (23) makes it meaningful to characterize the radiation yield by intergrating Eq. (23) over a small solid angle around θ_r. The spectral efficiency

$$\left(\frac{dN}{d\omega}\right)_r \equiv \int_0^{4\pi}\left(\frac{d^2N}{d\omega\, d\Omega}\right)_r d\Omega$$

can be evaluated by using the fact that the angular distribution is highly concentrated around $\theta = \theta_r$:

$$\left(\frac{dN}{d\omega}\right)_r \approx \frac{8\lambda^2\alpha}{\pi^2 cl}\frac{\sinh(\sigma_r-\rho)M}{\sigma_r-\rho} e^{-M(\rho+\sigma_r)} \times[|G_r\beta\Delta\varepsilon|\sin(l_2\pi/l)]^2, \tag{24}$$

where $\sigma_r \equiv \sigma(\theta - r)$, $G_r \equiv G(\theta_r)$. If $|G|$ is approximated with Eq. (5), one obtains

$$\left(\frac{dN}{d\omega}\right)_r = \frac{2\lambda\alpha}{\pi^2 c}\frac{\sinh[M(\sigma_r-\rho)]}{(\sigma_r-\rho)} e^{-M(\sigma_r+\rho)}\frac{\lambda}{l}|\Delta\varepsilon|^2 \times \sin^2(l_2 r\pi/l)\left|\frac{\beta\sin\theta_r(1-\beta^2-\beta\cos\theta_r)}{(1-\beta^2\cos^2\theta_r)(1-\beta\cos\theta_r)}\right|^2. \tag{25}$$

Choosing $l_2 = r^{-1}l(m+\frac{1}{2})$ where m is an integer, $m<r$, and substituting resonant condition, Eq. (1), into Eq. (25), we transform the expression to the formula that does not depend on θ_r:

$$\left(\frac{dN}{d\omega}\right)_r = \frac{2\alpha\lambda}{\pi^2 cr^4}|\Delta\varepsilon|^2\frac{\sinh[(\sigma_r-\rho)M]}{\sigma_r-\rho}\frac{\lambda}{l} \times\exp[-M(\sigma_r+\rho)] \times\frac{(r-\beta l/\lambda)^2[1-(\beta^{-1}-r\lambda/l)^2]}{(2-r\beta\lambda/l)^2}. \tag{26}$$

The main mechanism competing with the TR radiative process is bremsstrahlung. We, however, expect bremsstrahlung in the soft-x-ray domain (1–200 Å) to be negligibly small in the vicinity of resonant radiation peaks. Indeed, using [17,18] and taking photoabsorption into consideration, one obtains the bremsstrahlung efficiency in the energy domain of interest, $E_0 > 200$ keV, as

$$\frac{dN_{\rm br}}{d\omega} \approx 4Z^2\alpha r_e^2(\omega\bar{\mu})^{-1}N_A L[\tfrac{4}{3}\ln(183Z^{-1/3})+(\tfrac{1}{9})] \times[1-\exp(-\bar{\mu}L)], \tag{27}$$

where L is the total length of the medium. To compare the efficiency of TR and bremsstrahlung, we introduce the normalized TR efficiency as

$$\eta_{\rm TR} = E_0^{-1}\left(\frac{dN}{dE_{\rm ph}}\right)_{r=1}. \tag{26'}$$

Here E_0 is in MeV and $E_{\rm ph} = \hbar\omega$ is the photon energy in eV, so that η is the number of photons generated by one electron per 1 eV of photon energy per 1 MeV of electron energy. [It is conventional to measure TR efficiency per 1 eV of photon energy rather than per unit frequency as is common in theory. Introduced in Eq. (26′), additional normalization with respect to the electron energy addresses, in fact, the cost of using high-energy beams.] In a typical case, $L \sim 10$ μm, $\lambda \sim 16$ Å, and Ba as a radiator, Eq. (27) yields $\eta_{\rm br} = E_0^{-1}(dN_{\rm br}/dE_{\rm ph}) \sim 10^{-9}$ for $E_0 = 4.5$ MeV. On the other hand, Eq. (26) for TR at the *absorption edge* (see Sec. III) gives $\eta \sim 10^{-7}$ for the same example (see also Sec. VI), i.e., two orders of magnitude higher. Far from absorption edges, or when TR vanishes, however, the bremsstrahlung radiation cannot be neglected. Although TR is much stronger than the bremsstrahlung in the vicinity of most of the resonant peaks at absorption edges, we will always account for the bremsstrahlung contribution to the total radiation.

III. RESONANCES OF THE DIELECTRIC CONSTANT AT THE ATOMIC X-RAY ABSORPTION EDGES

The TR differential efficiency, Eq. (3), is directly proportional to $|\varepsilon_1 - \varepsilon_2|^2$; the photoabsorption coefficient $\bar{\mu}$ in Eq. (20) or (22) also effects the intensity of radiation appreciably.

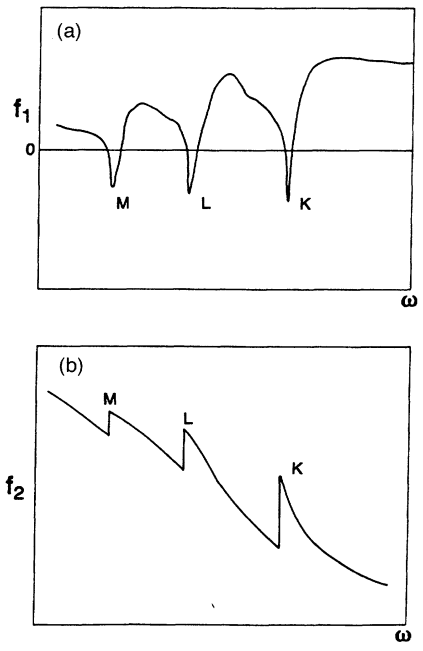

FIG. 4. Typical behavior of (a) atomic scattering factor f_1 and (b) atomic scattering factor f_2 vs frequency ω.

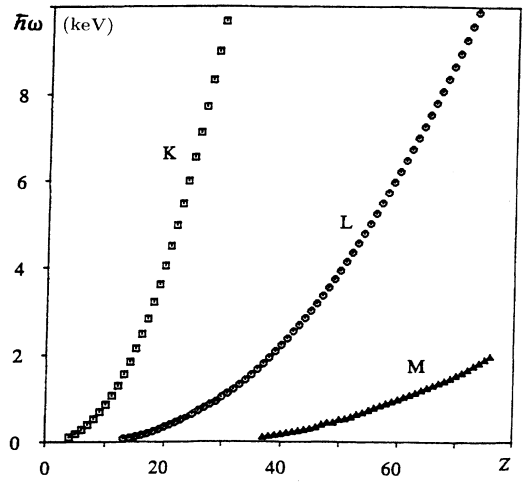

FIG. 5. K, L, and M absorption edge energy $\hbar\omega$ vs atomic number Z.

Both of these parameters undergo large change near so-called absorption edges, i.e., at the frequencies at which the absorption rises sharply [see Figs. 4(a) and 4(b)]. In Figs. 4(a) and 4(b) the atomic scattering factors f_1 [related to dielectric constant by Eq. (33)] and f_2 [related to the photoabsorption by Eq. (34)] versus photon energy are depicted. Because of the dramatic changes in f_1 and f_2, one must expect a significant resonant increase of TR intensity in at absorption edges of both the materials. For each particular element, these absorption edges, as well as related resonances of the refractive index, are due to the photoionization of bound electrons [25–27]. Its major feature is an almost discontinuous jump of absorption μ (or f_2, see below) as the photon energy approaches the binding energy of K, L, M, or N electrons (which are called K, L, M, N absorption edges, respectively). The most pronounced absorption edges correspond to inner atomic shells. Most of the elements have at least one absorption edge in the soft-x-ray domain. Figure 5 shows the location of K, L, and M absorption edges versus the atomic number Z. Not reflecting splitting of L and M shells into subshells, Fig. 5 depicts the position of absorption edges as the energy of the subshell with the lowest binding energy, to give a general idea of how this location depends on Z; the other subshell energies can be found, e.g., in Refs. [15,26].

Much less used in the physics and technology of radiation sources is the phenomenon of a resonant anomalous dispersion of a real component of dielectric constant at absorption edges, which can result in quite a drastic change of refractive index [27]. For example, although the common notion is that the x-ray refractive index n is slightly smaller than unity (which is due to the "plasma" model, see below), the resonant dispersion at absorption edges can result in n being significantly larger than 1. The anomalous x-ray dispersion must substantially affect both Čerenkov and transition radiations, since the behavior of $n(\omega)-1$ (for the Čerekov radiation) or $n_1^2(\omega)-n_2^2(\omega)$ (for TR) determines the very existence of these phenomena. In this section, we discuss in more detail the theory of anomalous dispersion at absorption edges. In the TR theory, the x-ray dielectric constant ε is usually [3,4,8,9] calculated with the so-called plasma formula

$$\varepsilon_i = 1-(\omega_i/\omega)^2, \quad i=1,2 \tag{28}$$

where $\omega_i = 2c\sqrt{\pi r_0 N_{ei}}$ is the plasma frequency, and N_{ei} $(i=1,2)$ is the number density of free electrons. It is also assumed [3–9] that *all* the atomic electrons respond to the x-ray radiation as if they were free, i.e., $N_{ei}=N_{Ai}Z_i$, where N_{Ai} are the number density of atoms in each medium and Z_i are atomic numbers. According to Eq. (28), the dielectric constant from this formula does not have any resonances and is always *smaller than unity* at $\omega \gg \omega_i$. This formula, however, is invalid at absorption edges, due to anomalous dispersion. One of the most drastic manifestations of the anomalous dispersion is the possibility for the refractive index n in the x-ray domain to be *larger than unity* at the absorption edges [15,26,27].

To account for the anomalous dispersion, we calculate the dielectric constant and absorption in terms of the complex atomic scattering factor, f:

$$\varepsilon = [1-fr_e\lambda^2 N_A/(2\pi)]^2, \quad f=f_1+if_2 \tag{29}$$

where factors f_1 and f_2 are real and can be expressed as [15,26]

$$f_1 = Z+\frac{1}{2\pi^2 r_e c}\sum_q \int_{\omega_q}^{\infty} \frac{\nu^2(\omega^2-\nu^2)Z_q\mu_q(\nu)d\nu}{(\omega^2-\nu^2)^2+\Gamma_q^2\omega^4} \tag{30}$$

and

$$f_2 = \frac{1}{2\pi^2 r_e c}\sum_q \int_{\omega_q}^{\infty} \frac{\Gamma_q\omega^2\nu^2 Z_q\mu_q(\nu)d\nu}{(\omega^2-\nu^2)^2+\Gamma_q^2\omega^4}. \tag{31}$$

Here Z_q is the number of q-shell electrons, μ_q is the cross section for photoionization of q-shell electrons by a photon with a frequency ν, ω is the frequency of the incident photon, Γ_q is the damping factor, and ω_q is the threshold (i.e., absorption edge) frequency. Γ_q is usually determined experimentally. If damping is due to spontaneous radiation only [26], one has

$$\Gamma_q = \Gamma_0 = 2e^2\omega_q/(3m_0c^3) = 2r_e k_q/3. \tag{32}$$

Equations (30) and (31) are essentially Kramers-Kronig relations for atomic scattering factors. Each bound electron in an atom can be treated as an oscillator and the summation of the scattering factors from each electron gives the resulting atomic scattering factor in Eqs. (30) and (31). Far from absorption edges, Eqs. (30) and (31) can be reduced to

$$f_1 = Z+\frac{1}{2\pi^2 r_e c}\int_0^{\infty} \frac{\nu^2\mu_a(\nu)d\nu}{\omega^2-\nu^2}, \tag{33}$$

$$f_2 = \omega\mu_a(\omega)/(4\pi r_e c), \tag{34}$$

where $\mu_a=\mu/(N_A)=\Sigma\mu_q Z_q$ is the atomic cross section. Even in this simplified form, f_1 departs significantly from the atomic number Z, i.e., from "plasma formula," Eq. (28), with $N_e=ZN_A$. Since usually $f_1 \gg f_2$ and $1 \gg r_e\lambda^2 N_A f_1/(2\pi)$, we can further simplify Eq. (29) as

$$\varepsilon \approx 1 - \pi^{-1} r_e \lambda^2 N_A f_1 . \tag{35}$$

Equation (35) coincides with Eq. (28) if we replace plasma frequency ω_i with the parameter ω_{ai} where $\omega_{ai} = 2c\sqrt{\pi r_e N_{Ai} f_{li}}$. With experimental and theoretical data for atomic scattering factors in Ref. [15], we can readily evaluate the absorption coefficient and dielectric constant with Eqs. (33) and (34), and make the following observations. As expected, we find $f_1 \approx Z$ at the frequencies above the K edge since all the electrons can then be considered as free. K edges of the elements with $Z=1$ to 4 lie below 0.2 keV, Fig. 5; therefore, we can evaluate their dielectric constants for photon energy $E_{\rm ph} > 0.2$ keV, using the plasma frequency ω_i. Since, however, many absorption edges of high-Z elements fall within the soft-x-ray domain, as depicted in Fig. 5, Eq. (35) has to be used now for calculating the dielectric constant. Due to anomalous dispersion, this constant can be larger than unity near the absorption edges.

To evaluate x-ray dispersion near absorption edges, we will use, instead of plasma formula, atomic scattering factors. Following Ref. [26], in particular assuming

$$\mu_q \sim (\nu/\omega_q)^{-p_q} \quad \text{for} \quad \nu < \omega_q , \tag{36}$$

where $2 < p_q < 3$ for most shells and frequencies, we rewrite Eq. (30) in the form

$$f_1 = \sum_q Z_q \, \mathrm{Re}(J_q), \quad q = K, L, \ldots \tag{37}$$

where

$$J_q = (p_q - 1) s^2 \int_1^\infty \frac{dx}{x^{p_q}(s^2 - x^2 - i\Gamma_q s^2)},$$

$$s = \omega/\omega_q , \quad x = \nu/\omega_q . \tag{38}$$

For K electrons, whereby $p_K \approx 3$ [26], we find

$$\mathrm{Re}(J_K) \approx 1 + \frac{1}{2s^2} \ln\left[\frac{(s^2-1)^2 + \Gamma^2}{1+\Gamma^2}\right], \tag{39}$$

whereas for L electrons, $p_L \approx 2$, we find

$$\mathrm{Re}(J_L) \approx 1 + \frac{1}{4s} \ln\left[\frac{(s-1)^2 + \Gamma^2/4}{(s+1)^2 + \Gamma^2/4}\right]. \tag{40}$$

For M electrons, $p_M \approx 2.5$ [24,25]; calculations for this and some other fractional values of p, $2 < p < 3$, yield much more complicated results [26] compared with Eqs. (39) and (40). At this point, however, such complications of p factor do not seem very imperative. We will assume here $p=2$ and use Eq. (40) for all the shells other than the K shell (thus slightly underestimating the magnitude $|f_l|$, and, therefore, the maximum TR intensity).

The photoionization gives rise to sharp resonances only when electrons are removed from the inner shells. Therefore, K shells can be used for any element beginning from $Z=3$, i.e., from lithium whose K-absorption edge corresponds to $\lambda_K \approx 226.5$ Å; λ_K decreases as Z increases. The L shells can be used beginning from $Z=14$ (silicon, with the L-absorption edge at $\lambda_L \approx 123$ Å), M shells beginning from $Z=48$ (cadmium, with $\lambda_M \approx 28.13$ Å), and N shells beginning from $Z=58$ (cerium, with $\lambda_N \approx 100$ Å; in this particular case, the N-shell resonance according to data [15] becomes very sharp even before the N shell is completely filled up). For all these cases, at the absorption edge, according to Eqs. (37)–(40), f_1 can be written approximately as

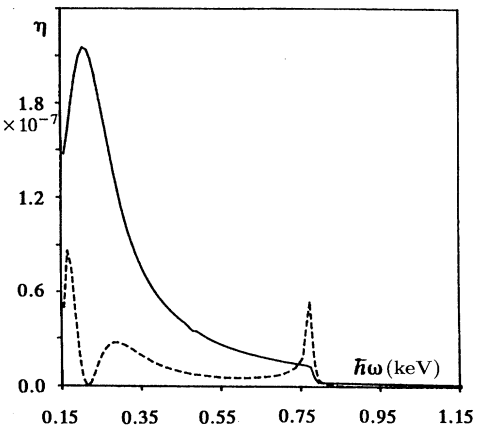

FIG. 6. Normalized TR efficiency η in number of photons per electron per 1 eV photon energy per 1 MeV electron energy vs photon energy $\hbar\omega$ in keV: Be/Ba nanostructure, $E_0 = 1$ MeV. The curve in the solid line is calculated with the plasma frequency formula, Eq. (28), while the curve in the dashed line is calculated with the atomic scattering factors, Eq. (35).

$$f_1 \approx Z - A_q + B_q[J_q(\omega/\omega_q) - 1], \tag{41}$$

where $A_q = 0$, 2, 10, 28 and $B_q = 2$, 8, 18, 32, for the K, L, M, and N shells, respectively. We have evaluated TR for a few specific combinations of materials using Eqs. (33)–(37) (see Sec. VI). Although the increment p_q is not very well defined for L, M, or N shells, the total error in the peak intensity of radiation with $p=2$ should not exceed 10–20 %. We have not accounted for the splitting of the higher shells (L,M,N) into subshells, which should reduce the resonance peak of $|f_1|$ and therefore the peak intensity of the TR. Further calculations are required for these shells; it should be noted, however, that the peak resonant magnitude of f_1, Eqs. (39) or (40), is insensitive to deviations of Γ from purely radiation damping, Eq. (32), since this magnitude at the point of resonance, $s=1$, depends on Γ as $\sim \ln\Gamma$.

By the very nature of absorption edges, the absorption is weak at the frequencies just below an absorption edge, and strong just above it. This leads to the further narrowing of a resonant line of the TR, since almost half of the resonant line originated by the resonance of the refractive index is cut off by a change of absorption [the intensity of radiation depends on μ as $\exp(-\bar{\mu} l)$]. The resulting narrow peaks are shown by the dashed curve in Fig. 6; for comparison, the spectral distribution from calculation with plasma frequency is shown by the solid curve. One can see that more narrow peaks occur in the dashed curve calculated with atomic scattering factor f, Eq. (35).

IV. SELECTION OF MATERIAL COUPLES FOR NARROW-LINE TR

Although the proposed technique can be used to generate broad-spectrum radiation in the entire x-ray domain, the most efficient use of the TR in solid-state nanostructures is to generate *narrow*-line x-ray radiation at the absorption edges of components, where dielectric constant ε changes drastically. The idea is that for each desired frequency, one of the materials is chosen to have its absorption edge in the close vicinity of that frequency. We will call such layers "radiators." The alternating material must then be chosen to have its absorption edges far from that frequency; we will call such layers "spacers." Another requirement for the spacer is that its absorption at the desired frequency be weak. This brings us to the condition that for most of the TR frequencies the spacer must be a light element with a low atomic number. Yet another, "technological" requirement for each material is its ability to form stable layers with smooth surfaces. All these requirements single out the "island of light elements"—the three light elements B, Be, and C—as the best potential spacers. It is worth noting that C is conventionally used in x-ray multilayer mirrors [13].

We illustrate selecting absorption edges for radiators using Fig. 5 where the photon energies of K, M, L absorption edges are plotted against the atomic number of elements (the data are taken from Ref. [15]). One can see that for photon energy up to 2 keV, a radiator can be chosen from K, L, or M branches. The further selection of one of these branches is based on the absorption factor as well as the dielectric constant factor $(\varepsilon_1-\varepsilon_2)^2$. At photon energy higher than $\sim$0.3 keV ($\lambda\lesssim 44$ Å), the rule of thumb is to choose the heaviest element as the radiator because its dielectric constant differs most from that of the light spacer. To illustrate that, consider a photon energy $\sim$0.88 keV (with $\lambda\approx 14$ Å). One can see from Fig. 5 that the radiator candidates are Ni and Ce (leaving aside Ne as a gas), Ce being best. In general, a radiator must be selected by an optimization process (see the next section). A typical example of narrow TR spectra is shown in Fig. 10 for nanostructures with Ba as the radiator and Be or C as the spacer (see more detailed discussion in Sec. VI).

The above described procedure enables one to select couples of heavy (radiator) and light (spacer) materials for relatively high photon energies, or short wavelengths (down to a few angstroms or even shorter). At the lower photon energies, however, a light element may become a good radiator too. Consider an example when the desired photon energy is 113 eV ($\lambda\approx 110$ Å). One can see from Fig. 5 that radiator candidates are Be (K shell), Al (L shell), and Rb (M shell). Since at low photon energy the absorption is stronger for the higher atomic number, Be is the best candidate. It is obvious, therefore, that in order to design a narrow-line radiator for longer wavelengths ($\geqslant 44$ Å) one has to use couples of two materials out of the "island of light elements," i.e., B, Be, or C. A combination of any two of these materials will radiate at two wavelengths (energies) out of the three: 43.68 Å (284.84 eV) for C, 66.0 Å (188.0 eV) for B, and 111.0 Å (111.7 eV) for Be. Which one of these two lines is stronger depends on the design of the system (see the next section). The electron energy required for these structures is very low, from 200–300 keV to 1 MeV.

V. OPTIMIZATION PROCEDURE

Provided that the materials for both the radiator and spacer have been selected, the next step in designing an efficient radiation system is to choose the geometry of the nanostructure (the spatial period and total length) to maximize TR intensity for a given frequency and electron energy. Such a procedure should also determine the spatial angle of the maximum TR intensity. In this section we outline the approach for evaluating the optimal spatial period $l_{\rm opt}$ and the optimal total length $L_{\rm opt}$ (or the optimal total number of layers, $M_{\rm opt}$) required to obtain maximum radiation. We will also discuss (i) the minimum electron energy below which the power of radiation is severely limited by electron scattering, and (ii) the maximum ("ceiling") electron energy, which is due to the photoabsorption.

In this section we consider only the main spatial mode, $r=1$ [note that the TR power decreases as r^4, Eq. (26)] and choose $l_1=l_2=l/2$, so that in Eq. (25), $\sin^2(\pi l_2/l)=1$. We use Eq. (25) or (26) to evaluate the spectral efficiency $dN/d\omega$ as a function of the spatial period, l, and the number of layers M for a given wavelength λ and electron energy E_0.

Note first that due to the very nature of resonant TR, the TR differential efficiency, Eq. (2), is factorized in such a way that the total length L (or the total number of layers M) affects only one factor, F_3, in Eq. (2) [see Eq. (11) and Sec. II]. This allows us to optimize the TR differential efficiency with respect to L or M, using only that factor. Using here spectral efficiency, $dN/d\omega$ [see Eqs. (24)–(27)], we separate out a resonant enhancement factor

$$P\equiv 2\sigma\,\sinh[(\sigma-\rho)M]\exp[-M(\sigma+\rho)]/(\sigma-\rho)$$

in Eq. (25) or (26), which is due to factor F_3 of Eq. (2), optimize it with respect to M, and obtain the optimal number of layers $M_{\rm opt}$ as

$$M_{\rm opt}=\ln(\sigma/\rho)/2(\sigma-\rho),\quad L_{\rm opt}=lM_{\rm opt}, \tag{42}$$

and

$$P_{\rm opt}=(\rho/\sigma)^{\rho/(\sigma-\rho)}. \tag{42'}$$

(Be reminded that $\sigma=\bar{\mu}/2l\,\cos\theta$ and $\rho=l/2L_{\rm cr}$.) The existence of a maximum in the TR efficiency at a certain (optimal) total length is evident from Fig. 7, which depicts the variation of radiation efficiency with the total length $L=Ml$. This maximum is explained by the competition of two factors: the photoabsorption which gives rise to the saturation of the TR efficiency at a short length $L\approx 1/\bar{\mu}$, and the electron scattering which takes over at $L\approx L_{\rm cr}$ so that TR drops abruptly when $L>L_{\rm cr}$. Figure 7 shows that the effect of the photoabsorption is stronger than the effect of the electron scattering since the absorption length $\bar{\mu}^{-1}$ is of the order of a micrometer [15] while the critical length $L_{\rm cr}$ is of the order of a millimeter [16] for $E_0\approx 1$ MeV and $\lambda\approx 10$ Å. The photoabsorption is even stronger in materials with high atomic numbers [15]. Thus, typically, $\sigma\gg\rho$, and since also $\cos\theta\approx 1$, Eq. (42) can be written as

$$M_{\rm opt}\approx\ln(\bar{\mu}L_{\rm cr})/\bar{\mu}l,\quad L_{\rm opt}\approx\ln(\bar{\mu}L_{\rm cr})/\bar{\mu}. \tag{42''}$$

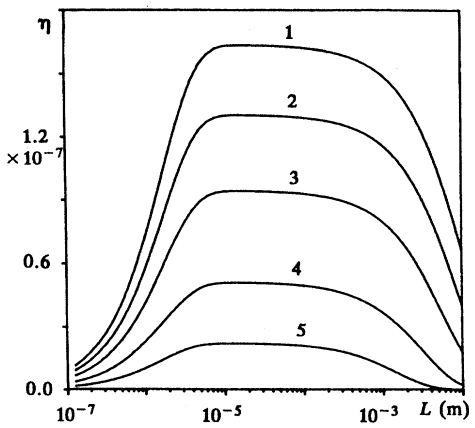

FIG. 7. Normalized TR efficiency η vs the length of the radiating structure, L, in m at $\lambda \sim 17$ Å for the combination of Be/Ba at various electron energies E_0 (curve 1, $E_0 = 4$ MeV; curve 2, 3 MeV; curve 3, 2 MeV; curve 4, 1 MeV; and curve 5, 0.5 MeV).

In the periodic structure with optimized number of layers, $M = M_{\text{opt}}$, the spectral efficiency, Eq. (25) or (26), is

$$\left(\frac{dN}{d\omega}\right)_{r=1} = (2\pi^2 c\bar{\mu})^{-1}\alpha|\Delta\varepsilon|^2 P_{\text{opt}} Q, \tag{43}$$

where

$$Q = \cos\theta_1 \left[\frac{\sin\theta_1(1-\beta^2-\beta\cos\theta_1)}{(1-\beta^2\cos^2\theta_1)}\right]^2. \tag{44}$$

These equations allow one to further optimize the spectral efficiency with respect to the resonant angle θ_1 or spatial period l, which are related to each other by Eq. (1). In the typical case of photoabsorption dominating over electron scattering, $\sigma \gg \rho$, we have $P_{\text{opt}} \approx 1$ [see Fig. 8(c)], and θ_1 or l affect only the factor Q. The numerically calculated ratio l_{opt}/λ that optimizes Q, and respective Q_{opt}, versus the energy of the electron beam, $E_0 = mc^2(\gamma - 1)$, are shown in Fig. 8(a). For sufficiently high electron energy $[\gamma^2 \gg 1, \theta_1^2 \ll 1, \lambda/l \approx (\theta_1^2 + \gamma^{-2})/2 \ll 1]$, the factor Q is approximated by a very simple formula:

$$Q \approx \frac{\theta_1^2}{(\gamma^{-2}+\theta_1^2)^2} \approx \frac{l}{2\lambda}\left(1 - \frac{l}{2\lambda\gamma^2}\right). \tag{45}$$

Examination of Eq. (45) and Fig. 8(a) shows that for sufficiently high electron energy (e.g., $E_0 > 1$ MeV), optimized factor Q_{opt} and respective l_{opt} (and θ_{opt}) are

$$l_{\text{opt}}/\lambda \approx \gamma^2, \quad Q_{\text{opt}} \approx \gamma^2/4, \quad \theta_{\text{opt}} \approx \gamma^{-1}. \tag{45'}$$

Comparing Eq. (45′) for l_{opt} with Eqs. (10)–(10″), it is easy to see the connection between l_{opt} with the transformation length a_i,

$$l_{\text{opt}} \approx \pi a_{\text{opt}} \approx \lambda\gamma^2.$$

For a fixed spatial period, as the electron energy increases, Q saturates [8] after Q_{opt} is reached. In Fig. 8(b), the emission angle θ_{opt} for optimal structure is ~ 1 rad for $E_0 < 100$ keV. After a drastic drop at $E_0 \sim 200$ keV, θ_{opt} reduces to ~ 0.03 rad at $E_0 \sim 100$ MeV. Abrupt changes (jumps) in l_{opt} and Q_{opt} near $E_0 \sim 200$ keV are caused by the splitting of the radiation pattern G into two lobes at $E_0 = 138.7$ keV (see Sec. I and Fig. 2). Estimated energy at which the splitting appears first, differs somewhat from the location of the jump in Figs. 8(a) and 8(b) since that estimate is obtained under the assumption of zero emission angle θ. The factor P_{opt} vs ρ/σ in Eqs. (43) and (44) is plotted in Fig. 8(c). P_{opt} is close to unity for $\sigma \gg \rho$ and to zero for $\rho \gg \sigma$. Typically, $\sigma \gg \rho$, so that Eq. (43) reduces to

$$\frac{dN}{d\omega} = (\alpha/2\pi^2 c)|\Delta\varepsilon(\lambda)|^2 Q(\theta)/\bar{\mu}(\lambda), \tag{46}$$

useful for practical purposes; or, when $E_0 > 1$ MeV,

$$\frac{dN}{d\omega} \approx (2\alpha/\pi^2 c)|\Delta\varepsilon|^2/\gamma^2\bar{\mu}. \tag{46'}$$

Let us discuss the maximal possible energy ("ceiling") of an electron, which is imposed by the photoabsorption and electron scattering. It is obvious from the preceding discussion that it is meaningless to use a structure with $M > M_{\text{opt}}$, or $L > L_{\text{opt}}$. On the other hand, in order to still have a *multilayer* structure with, say, $M \geq 10$, one has to impose the critical condition for the maximum spatial period of the nanostructure, $l \leq L_{\text{opt}}/10$. Using this consideration as well as Eq. (45′) for $l = l_{\text{opt}}$, we obtain the ceiling of the required electron energy as

$$\gamma \leq \gamma_{\text{opt}} = \sqrt{\ln(\bar{\mu}L_{\text{cr}})/10\lambda\bar{\mu}}. \tag{47}$$

For typical values of $\bar{\mu}^{-1}$ μm and $L_{\text{cr}} \sim 1$ mm at $\lambda \approx 10$ Å we obtain $\gamma \approx 26.5$, i.e., $(E_0)_{\text{ceil}} \sim 13$ MeV. This is the highest meaningful energy to be used in this case; the energies lower by a factor of 2 are still close to the optimal regime. These energies are within reach of many readily available small-scale accelerators. (Note also that these energies are far below the critical Čerenkov energy in the x-ray domain.) At higher photon energies, e.g., $\hbar\omega \sim 30$ keV ($\lambda \sim 0.4$ Å), as in Sec. VII, $\bar{\mu}$ can decrease by almost two orders of magnitude, which would allow for higher electron energies.

The minimum electron energy required to obtain appreciable TR intensity is achieved when the electron scattering results in the same losses as photoabsorption does, i.e., when $L_{\text{cr}} = 1/\bar{\mu}$. Typically, $1/\mu$ is of the order of micrometers at $\lambda \sim 10$ Å (see Fig. 9 that shows critical length versus electron energy for various combinations of materials). The critical length L_{cr} is, however, not the best parameter for comparison with the photoabsorption length, since L_{cr} corresponds to a completely vanishing electron beam. Instead, the quantity L_{cr}/e would be a more reasonable reference scale for such a purpose. For example, when $L_{\text{cr}}/e \approx 5$ $\mu\text{m} \approx 1/\bar{\mu}$, $E_0 \sim 70$–100 keV can be regarded as the minimum required energy; above this energy, the photoabsorption dominates over electron scattering. It is also worth noting that the radiation pattern changes rapidly (see Sec. I) in the same range of electron energy.

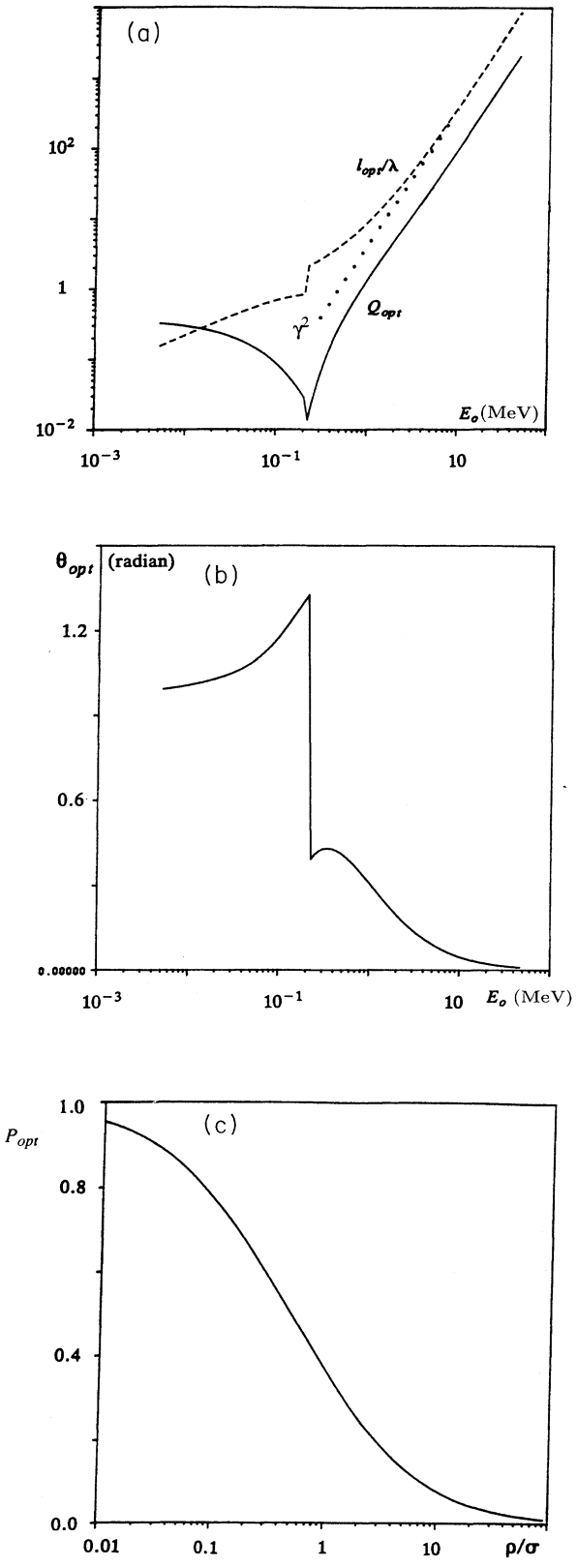

FIG. 8. (a) Optimal normalized spatial period l_{opt}/λ (dashed line), and parameters Q_{opt} (solid line) and γ^2 (dotted line) vs the incident electron beam energy E_0, (b) emission angle θ_r in radians vs E_0, and (c) the factor P_{opt} vs ρ/σ.

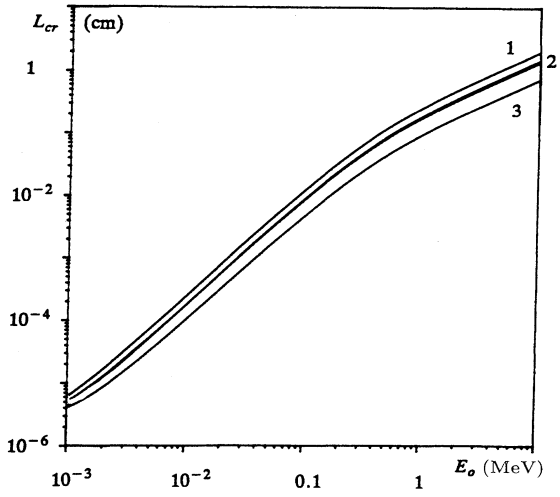

FIG. 9. Critical length L_{cr} in cm vs incident electron energy E_0 in MeV for the following combinations: curve 1, C/Ba; curve 2, C/Eu and C/Ge; and curve 3, C/Ta.

VI. EXAMPLES OF MATERIAL COUPLES

In this section we consider some material couples to illustrate designing periodic nanostructures for efficient generation of narrow-line TR. In these examples, the spacer is made of carbon (C) or beryllium (Be). The advantage of C is its surface smoothness and stable boundary separation, while Be, with its K edge being at sufficiently low energy, has low absorption losses in the soft-x-ray domain; the K edges of C and Be are at 0.283 and 0.111 keV, respectively. For the sake of illustration, we choose barium (Ba), cerium (Ce), europium (Eu), and germanium (Ge) as radiators. In general, the choice of a radiator depends on the frequency range desired (see Sec. IV). The absorption edges of Ge, Ba, Ce, and Eu are at 1.217 keV (L edge), 0.780 keV (M edge), 0.883 keV (M edge), and 1.127 keV (M edge), respectively. These elements with high atomic number have large f_1 and f_2 factors compared to those of elements with low atomic number. The results of the previous sections indicate that in a soft-x-ray domain the TR spectra density should have two peaks. The low-frequency peak is due to the component with low atomic number (a spacer), while the high-frequency peak is due to the component with higher atomic number (a radiator). For TR to be much stronger than bremsstrahlung, in our examples we choose the electron beam energy to be 4.5 MeV; such energy is readily available from commercial electron accelerating devices, see Sec. VII.

Figure 10 depicts radiation efficiency $\eta = \eta_{\text{TR}} + \eta_{\text{br}}$ versus photon energy for the typical nanostructures Be/Ba and C/Ba. TR from each structure is optimized at the absorption edge frequency of the radiator, Ba. Since the TR peaks are very narrow, Fig. 10 depicts only the portion of each spectrum near the radiator absorption edge, where we used Eq. (41) for f_1. It is obvious that the spectrum peaks at the radiator absorption edge frequency. The location of the high-frequency peak does not depend on the choice of the spacer, whereas this choice affects the intensity of radiation. We notice that the structure with the Be spacer shows higher radiation peak, which is due to larger $|\Delta\varepsilon|$. Since the TR intensity

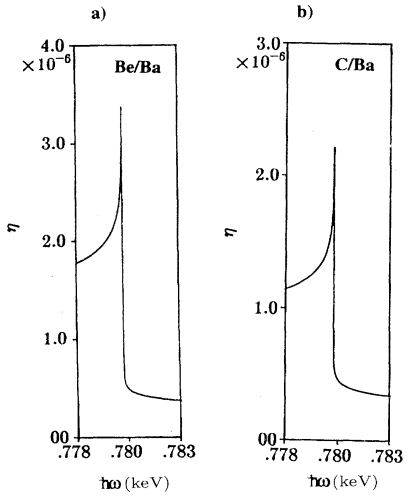

FIG. 10. Normalized radiation efficiency $\eta = \eta_{TR} + \eta_{br}$, with bremsstrahlung radiation included, in number of photons per electron per 1 eV photon energy per 1 MeV electron energy vs photon energy $\hbar\omega$ in keV, for the nanostructures made of (a) Be/Ba, and (b) Be/C. $E_0 = 4.5$ MeV, and the spatial period l and total length L are optimized at the Ba absorption edge.

is proportional to $|\Delta\varepsilon|^2$ which decreases as ω increases, the high-frequency peaks are lower than the low-frequency peaks. Similarly, we expect the lower-frequency TR in the light elements to be stronger than high-frequency TR in heavier elements. We also notice the abrupt decrease of TR above the absorption edge, which is due to the discontinuous jump of absorption.

The optimal parameters (total length L of the structure and its spatial period l) required to attain the maximum radiation for the C/Ba, C/Ce, C/Eu, and C/Ge nanostructures are listed in Table I along with radiation efficiency for TR, η_{TR}, and bremsstrahlung, η_{br}, and in Table II for the Be/Ba, Be/Ce, Be/Eu, and Be/Ge structures. The parameters L and l for the structures in Tables I and II correspond to those used in Fig. 10, i.e., to the structures optimized for the absorption edge of the heavier element. The emission angle which depends on the electron beam energy is approximately 0.573° for the case of $E_0 = 4.5$ MeV. For example, if the resonant peak of radiation at the wavelength $\lambda = 17$ Å is desired, we select the C/Ba structure and obtain its optimal parameters as $l \approx 1400$ Å with equally spaced layers, and $L_{opt} \approx 9$ μm at $E_0 = 4.5$ MeV. It is important to note that TR is two to three orders of magnitude stronger than the bremsstrahlung, whose contribution, therefore, can be neglected here.

When comparing our results, Tables I and II, with other results on TR, which are typically expressed (see, e.g., [5,6]) in terms of the number of photons per electron per sr, one should multiply η by E_0 in MeV (that is, by 4.5) and divide it by a very small spatial angle of emission; see Eq. (48) below. This would transform, e.g., $\eta_{TR} \approx 3.37 \times 10^{-6}$ from the first line of Table I into 0.3 photon/(electron×sr), which is substantially larger than the respective number obtained for nonoptimal structures experimented with so far [5,6].

An important practical question, which of the prospective pairs "radiator-spacer" can be technically realized, is outside the scope of this paper. It is important to notice, though, that multilayers that we considered, carbon and boron, have already been synthesized, and, furthermore, there is a reason to believe "that multilayers may be synthesized using a large fraction of the ninety-two naturally occurring elements for technical purposes" [13(b)].

VII. RESONANT TR SOURCES: POTENTIALS FOR APPLICATIONS

In this section we briefly address prospects for practical applications of resonant TR. We will do it by comparing its characteristics with those of x-ray sources already in use; in such a way, we will be able to arrive at some conclusions while not going into specific design (optics, etc.) of an application. The most common characteristic used to compare x-ray sources, as far as their applications are concerned, is spectral brightness B_S usually defined as the number of generated photons per second per 1 mm^2 source surface per 1 mrad^2 spatial angle in 10^{-3} relative bandwidth [28] (almost as often, B_S is referred to as spectral brilliance [29]). Since TR is confined to the close vicinity, $\delta\theta \ll 1$, of the resonant emission angle $\sim\theta_r$ (we consider here only the lowest TR mode, $r = 1$), the small angle $\delta\theta$ is determined by the resonant factor F_3, Eqs. (11) and (14). Using Eq. (11) for simplicity, one can see that most of TR with $r = 1$ would propagate within $|X(\theta) - \pi| < \sqrt{2}/M$; thus the range of emission angles for this TR mode is $\delta\theta \approx (2\sqrt{2}/\pi\theta_{r=1})(\lambda/L_{opt})$. The respective spatial angle of emission, $\delta\Omega$, is

$$\delta\Omega \equiv 2\pi \sin\theta d\theta \approx 4\sqrt{2}\lambda/L_{opt}. \tag{48}$$

B_S can then be related to the TR normalized efficiency η, Eq. (26′), as

$$B_S \approx 10^9 (\delta\omega/\omega)(L_{opt}/\lambda) E_0 \eta J, \tag{49}$$

where $\delta\omega/\omega$ is the relative bandwidth of the resonant TR (typically $\sim 10^{-3}$ for the examples in Tables I and II, see

TABLE I. The optimal spatial period l_{opt}, radiation efficiency of TR η_{TR} and of bremsstrahlung η_{br}, and optimal total length L_{opt} for nanostructures made of Be/Ge, Be/Ce, Be/Ba, or Be/Eu at the TR peaks related to an absorption edge of the heavier element in each combination (the L edge for Ge, and M edges for the Ba, Ce, and Eu). $E_0 = 4.5$ MeV, the emission angle $\theta_1 = 0.573°$.

Radiator	λ (Å)	l_{opt} (Å)	L_{opt} (μm)	η_{TR}	η_{br}
Ba	16.90 (0.780 keV)	1329	13.8	3.37×10^{-6}	4.75×10^{-9}
Ce	14.04 (0.883 keV)	1269	7.2	1.80×10^{-6}	4.17×10^{-9}
Eu	11.00 (1.127 keV)	979	11.3	7.72×10^{-7}	4.50×10^{-9}
Ge	10.19 (1.217 keV)	988	10.2	1.33×10^{-6}	2.24×10^{-9}

TABLE II. The same as in Table I except that in each material couple Be is replaced with C.

Radiator	λ (Å)	l_{opt} (Å)	L_{opt} (μm)	η_{TR}	η_{br}
Ba	16.90 (0.780 keV)	1396	9.07	2.21×10^{-6}	3.19×10^{-9}
Ce	14.04 (0.883 keV)	1297	5.97	1.57×10^{-6}	3.55×10^{-9}
Eu	11.00 (1.127 keV)	982	9.48	7.17×10^{-7}	3.90×10^{-9}
Ge	10.19 (1.217 keV)	993	9.01	1.26×10^{-6}	2.09×10^{-9}

Fig. 10), E_0 is the electron energy in MeV, and J is the electron current density in A/mm^2. For a Ba/Be multilayer nanostructure optimized at $\lambda\approx16$ Å for a 4.5-MeV electron beam (see Table I), Eq. (49) yields $B_S\approx1.3\times10^{11}\,J$ photon s^{-1} mrad^{-2} mm^{-2} (0.1% bandwidth). Commercially available small-scale electron accelerators readily generate 0.5–4.5-MeV electron beams with dc of up to 100 mA (e.g., Dynamitron manufactured for electron processing of materials), or with pulse currents of up to 10 A in 1–10-μs pulses with a kHz repetition rate (rf accelerators used in radiation therapy) [30]. Since their beam diameter varies usually from 1 mm^2 to a few cm^2, dc densities of a few A/mm^2 or pulse current densities of a few hundred A/mm^2 are readily available from these accelerators. With such current densities, resonant TR multilayers would provide the average B_S of 10^9-10^{10}—much higher, in this spectral range, than the brightness of x-ray tube lines ($\sim10^6$) or bremsstrahlung sources ($\sim10^5$), and on a par with the average brightness of x rays from laser-produced plasma (LPP) (10^9-10^{10}) (see, e.g., [28,30]). Therefore, multilayer TR radiators optimized at absorption edges could be among the brightest laboratory (nonsynchrotron) x-ray sources, and compete with LPP in applications to, e.g., scanning x-ray microscopy.

A very promising application of multilayer TR generators could be expected in computed tomography (CT). Ongoing research on CT using synchrotron radiation (see, e.g., [31]) demonstrates a number of advantages of synchrotron radiation over commonly used x-ray tubes. In particular, by taking two images at the two energies bracketing the K edge of iodine (33.17 keV), one can achieve very high contrast; this is called multiple-energy CT (MECT) [31]. Energy spread (linewidth) of the imaging x-ray beam should be sufficiently small, preferably $\sim0.1\%$. An experimental MECT system [31] employs the photon flux of $\sim2\times10^8$ photons/s with E_{ph} near the iodine K edge. Although all the particular examples of radiating structures given so far have been optimized to radiate at photon energies near 1 keV, the TR photon energy of tens of keV is well within the scope of our consideration.

To bracket the K edge of iodine, one could use, e.g., Ba (K edge at 35.41 keV) and Te (31.81 keV) as radiators. The Ba K edge is not the closest to iodine's from above, but closer elements Xe and Cs do not seem appropriate for a multilayer; however, Ba will provide enough contrast, since the absorption coefficient of I at the Ba K edge is four times larger than at the Te K edge [32]. The pilot experiments can be done by using two separate nanostructures, e.g., Ba/C and Te/C. Our estimates based on the results of Secs. II and III, and using electron energy $E_0\sim9.5$ MeV (i.e., $\gamma\sim10$), and wavelength ~0.375 Å, give an optimal spatial period, Eqs. (45′), of $l_{opt}=\lambda\gamma^2\approx150$ Å; using the data [15,16,32] for Ba/C, $\bar{\mu}\sim30$ cm^{-1} and $L_{cr}\sim2$ cm, we obtain the optimal number of layers, Eq. (42″), of $M_{opt}\sim0.9\times10^5$, which corresponds to an $L\sim1.4$ mm thick nanostructure. Our estimates also show that one may expect the photon flux to be of the same order of magnitude (or even larger) as the flux given in Tables I and II, and therefore sufficient for an experimental MECT system.

Interestingly, since for this particular application we need the radiation at *two* frequencies that are relatively close to each other, we can have the advantage of combining both radiators, Ba and Te, into *one* nanostructure (without "idle" spacers like B, Be, or C), which could then be optimized for both lines simultaneously. The disadvantage of such a combination will be that since the K shell of Te is at a longer wavelength than that of Ba, the radiation at the Ba K shell will be on the strongly absorbing side of the absorption edge of Te (while the Te K-shell line will be on the weakly absorbing side of the absorption edge of Ba). However, our estimates show that even so, this structure can have a radiation output of the same order of magnitude, with the optimized parameters being $l_{opt}\sim145$ Å, $M_{opt}\sim4\times10^4$, and $L_{opt}\sim0.6$ mm.

One of the issues to be addressed in more detailed future research is possible damage to a nanostructure, which can be caused by both electron beam and generated x rays, with the former being usually much more relevant. We estimated, however, using [33], that the electron energy loss would be of the order of 10^{-3} eV per atom for $J\sim1$ A/cm^2 in a 1-μs pulse, which seems insignificant. Our estimates indicate, therefore, that TR radiation based on a solid-state nanostructure source for MECT systems can be potentially competitive with synchrotron radiation while being possibly much more affordable for a hospital or university.

CONCLUSIONS

We investigate the role of photoabsorption and electron scattering in x-ray TR emission by low-energy electrons in solid-state multilayer nanostructures. We showed that electron energy from ~200 keV to a few MeV is sufficient to generate narrow-line TR with a relative linewidth $\sim10^{-3}-10^{-4}$ in a nanostructure with a spatial period 100–1500 Å. We formulated the principle for selecting appropriate materials for both radiator and spacer to obtain narrow-line TR due to resonant anomalous dispersion of the refractive index at absorption atomic edges of various elements. We developed a procedure of designing nanostruc-

tures to generate maximum TR at a desired frequency, whereby the optimal spatial period, total length, and resonant angle are evaluated. Expected narrow linewidth and highly directional and very bright output could make nanostructures a competitive and possible much more affordable alternative to other x-ray sources for a number of applications in technology and medicine.

ACKNOWLEDGMENT

This work is supported by AFOSR.

[1] V. L. Ginzburg and I. M. Frank, Zh. Eksp. Teor. Fiz. **16**, 15 (1946) [Sov. Phys. JETP **9**, 353 (1945)].

[2] G. M. Garibyan, Zh. Eksp. Teor. Fiz. **60**, 39 (1971) [Sov. Phys. JETP **33**, 23 (1971)].

[3] M. L. Ter-Mikaelian, *High Energy Electromagnetic Processes in Condensed Media* (Wiley Interscience, New York, 1972).

[4] M. A. Piestrup, P. F. Finman, A. N. Chu, T. W. Barbee, Jr., R. H. Pantell, R. A. Gearhart, and F. R. Buskirk, IEEE J. Quantum Electron. **19**, 1771 (1983).

[5] P. J. Ebert, M. J. Moran, B. A. Dahling, B. L. Berman, M. A. Piestrup, J. O. Kephart, H. Park, R. K. Klein, and R. H. Pantell, Phys Rev. Lett. **54**, 893 (1985); M. A. Piestrup, J. O. Kephart, H. Park, R. K. Klein, R. H. Pantell, P. J. Ebert, M. J. Moran, B. A. Dahling, and B. L. Berman, Phys. Rev. A **32**, 917 (1985).

[6] M. J. Moran, B. A. Dahling, P. J. Ebert, M. A. Piestrup, B. L. Berman, and J. O. Kephart, Phys. Rev. Lett. **57**, 1223 (1986); M. A. Piestrup, D. G. Boyers, C. I. Pincus, Q. Li, G. D. Hallwell, M. J. Moran, D. M. Skopik, R. M. Silzer, X. K. Maruyama, D. D. Snyder, and G. B. Rothbart, Phys. Rev. A **45**, 1183 (1992).

[7] P. Goedtkindt, J.-M. Salome, X. Artru, P. Dhez, M. Jablonka, N. Maene, F. Poortmans, and L. Waritski, Nucl. Instrum. Methods Phys. Res. Sect. B **76**, 1060 (1991); V. V. Kaplin, V. N. Zabaev, E. I. Rosum, S. R. Uglov, and S. A. Voroblev, Phys. Lett. A **174**, 165 (1993); H. Backe, S. Gampert, A. Grendel, H.-J. Hartmann, W. Lauth, Ch. Weinheimer, R. Zahn, F. R. Buskirk, H. Euteneur, K. H. Kaiser, G. Stephan, and Th. Walcher, Z. Phys. A **349**, 87 (1994).

[8] M. L. Cherry, G. Hartmann, D. Muller, and T. A. Prince, Phys. Rev. D **10**, 3594 (1974).

[9] C. W. Fabjan and W. Struczinkski, Phys. Lett. **57B**, 483 (1975).

[10] A. E. Kaplan and S. Datta, Appl. Phys. Lett. **44**, 661 (1984); also in *Laser Techniques in the Extreme Ultraviolet*, edited by S. E. Harris and T. B. Lucatorto, AIP Conf. Proc. No. 119 (AIP, New York, 1984), pp. 304–310.

[11] S. Datta and A. E. Kaplan, Phys. Rev. A **31**, 790 (1985).

[12] A. P. Apanasevich and V. A. Yarmolkevich, Zh. Tekh. Fiz. **59**, 18 (1989) [Sov. Phys. Tech. Phys. **34**, 1237 (1989)]; **62**, 16 (1992) [**37**, 423 (1992)].

[13] (a) E. Spiller, in *Low Energy X-Ray Diagnostics*, edited by D. T. Attwood and B. L. Henke, AIP Conf. Proc. No. 75 (AIP, New York, 1981), pp. 124–130; (b) T. W. Barbee, Phys. Scr. **T31**, 147 (1990).

[14] C. T. Law and A. E. Kaplan, Opt. Lett. **12**, 900 (1987).

[15] B. L. Henke, E. M. Gullikson, J. C. Davis, At. Data Nucl. Data Tables **54**, 181 (1993).

[16] L. Pages, E. Bertel, H. Joffre, and L. Sklavenitis, At. Data **4**, 1 (1972).

[17] J. Ashkin and H. A. Bethe, in *Experimental Nuclear Physics*, edited by E. Sigre (Wiley, New York, 1953), Vol. 1.

[18] B. Rossi, *High-Energy Particles* (Prentice-Hall, Englewood Cliffs, NJ, 1961).

[19] In our calculations here we always assume that the x-ray radiation in the multilayer structure propagates without any retroreflection (Bragg reflection), since only the frequencies off Bragg resonances are of interest to us; at such frequencies, transmission is several orders of magnitude stronger than reflection. TR in the presence of Bragg reflection was considered recently in B. Pardo and J.-M. Andre, Phys. Rev. A **40**, 1918 (1989); M. S. Dubovikov, *ibid.* **50**, 2068 (1994).

[20] J. Dooher, Phys. Rev. D **3**, 2652 (1971).

[21] H. Raether, *Excitation of Plasmons and Interband Transitions by Electrons* (Springer-Verlag, New York, 1980), Chap. 4.

[22] C. T. Law and A. E. Kaplan, in *Short Wavelength Coherent Radiation: Generation and Applications*, edited by D. T. Attwood and J. Bokor, AIP Conf. Proc. No. 147 (AIP, New York, 1986), pp. 27–33.

[23] M. S. Longair, *High Energy Astrophysics* (Cambridge University Press, New York, 1992), Vol. 1.

[24] K. Kanaya and S. Ono, J. Phys. D **11**, 1495 (1978).

[25] E. Fermi, *Nuclear Physics* (University of Chicago Press, Chicago, 1950).

[26] L. G. Parratt and C. F. Hampstead, Phys. Rev. **94**, 1593 (1954).

[27] The physics of resonant anomalous x-ray dispersion and scattering (with the index of refraction being part of it) has been developed in great detail in the context of crystallography, starting from A. H. Compton and S. K. Allison, *X-Ray in Theory and Experiment* (Van Nostrand, New York, 1935); for an excellent recent collection of articles, see *Resonant Anomalous X-Ray Scattering. Theory and Application*, edited by G. Materlik, C. J. Sparks, and K. Fisher (North-Holland, New York, 1994). In particular, a detailed review of experimental data and earlier work are found in the papers by B. Lengeler, p. 35, R. L. Blake, J. C. Davis, D. E. Graessle, T. H. Burbine, and E. M. Gullikson, p. 79, and D. H. Templeton, p. 1.

[28] W. Sharf, *Particle Accelerators—Applications in Science and Technology* (Wiley, New York, 1989), 1.2.1 and 1.2.3.

[29] F. O'Neill, in *Laser-Plasma Interactions 4*, edited by M. B. Hooper (Institute of Physics and Physical Society, New York, 1989), pp. 285–315.

[30] R. H. Huebner, in *X-Ray and Inner-Shell Processes*, edited by T. A. Carlson, M. O. Krause, and S. T. Manson (APS, New York, 1990), pp. 161–169.

[31] W. Sharf, *Biomedical Particle Accelerators* (APS, New York, 1994), Chap. 6.

[32] E. B. Saloman, J. H. Hubell, and J. H. Scofield, At. Data Nucl. Data Tables **38**, 176 (1988).

[33] J. D. Jackson, *Classical Electrodynamics* (Wiley, New York, 1962), Eq. (13.13).